Corrosion Science 107 (2016) 41–48

Contents lists available at ScienceDirect

Corrosion Science

journal homepage: www.elsevier.com/locate/corsci

Localised corrosion in AA 2099-T83 aluminium-lithium alloy: The role of grain orientation

Y. Ma [a,*], X. Zhou [b,**], Y. Liao [c], Y. Yi [a], H. Wu [a], Z. Wang [a], W. Huang [a]

[a] College of Materials Science and Engineering, Chongqing University of Technology, Chongqing, 400054, PR China
[b] Corrosion and Protection Centre, School of Materials, The University of Manchester, Manchester M13 9PL, UK
[c] Chongqing University of Education, Chongqing, 400067, PR China

ARTICLE INFO

Article history:
Received 30 December 2015
Received in revised form 10 February 2016
Accepted 10 February 2016
Available online 11 February 2016

Keywords:
A. Aluminium
A. Alloy
B. SEM
B. TEM
C. Pitting corrosion

ABSTRACT

The mechanism for localised corrosion in AA 2099-T83 alloy during immersion in 3.5% NaCl solution is investigated. It is found that localised corrosion tends to occur in the grain with relatively large Schmid factor. The localised corrosion is related to selective dissolution of T_1 (Al_2CuLi) phase that preferentially precipitates at grain/subgrain boundaries and dislocations within grain interiors. A model is proposed to explain the development of the localised corrosion in the alloy by taking into account heterogeneous plastic deformation during cold working and preferential precipitation of T_1 phase at crystallographic defects within deformed grains.

1. Introduction

Aluminium-lithium (Al-Li) alloys are characterized by high specific strength and high specific modulus, which offer an opportunity for weight savings of aircraft and, thereby, the reduction of CO_2 emissions. Due to exceptionally reactive nature of lithium, the addition of lithium to aluminium alloy has triggered great interest of scientists on corrosion resistance of Al-Li alloys. Corrosion data is limited for the first generation Al-Li alloys but large amount of data has been generated for the second and third generation Al-Li alloys [1]. Kumai et al. [2] proposed that intergranular attack in commercial AA2090-T83E51 was strongly associated with the dissolution of copper-depleted zones that formed adjacent to grain and subgrain boundaries owing to local precipitation of copper-rich phases. Buchheit et al. [3] reported two types of pitting in AA 2090 alloy immersed in 3.5% NaCl solution, namely subgrain boundary pitting and constituent particle pitting. The subgrain boundary pitting was attributed to selective dissolution of T_1 (Al_2CuLi) phase at subgrain boundaries; the constituent particle pitting was ascribed to peripheral corrosion around the particle and propagation of corrosion along surrounding subgrain boundaries through selective dissolution of T_1 phase. The role of T_1 phase in localised corrosion of the alloy was further discussed based on a synthesized bulk T_1 intermetallic compound [4,5]. The work on the third generation Al-Li alloys such as AA 2050 [6–8] and AA 2099 [9–12] also indicated that increased precipitation of T_1 phase at grain/subgrain boundaries increased susceptibility of these alloys to localised corrosion.

Recently, two types of localised corrosion were observed in an AA2099-T83 alloy immersed in 3.5% NaCl solution. The first type localised corrosion, whose distribution is consistent with the distribution of constituent particles in the alloy, has been related to attack at and around the constituent particles [13]. The other type localised corrosion is characterized by corrosion product rings and hydrogen gas evolution at the corrosion site, with selective attack of grain/subgrain boundaries and particular grains. To date, however, a comprehensive understanding of the mechanism for the second type localised corrosion is still lacking. Hughes, Boag and coworkers [14–16] reported similar corrosion phenomena in an AA 2024-T3 alloy. They found that such localised corrosion in AA 2024-T3 alloy was related to clustering of intermetallic particles with opposite electrochemical activity (e.g. clustering of S-phase and Al-Cu-Fe-Mn particles). Nevertheless, recent work on AA 2099-T83 alloy indicated that neither was there clustering of intermetallic particles [17], nor was there individual constituent particles at the site of the second type localised corrosion [13]. The work of Guerin

* Corresponding author.
** Corresponding author.
E-mail addresses: myl@cqut.edu.cn (Y. Ma), xiaorong.zhou@manchester.ac.uk (X. Zhou).

doi:10.1016/j.corsci.2016.02.018

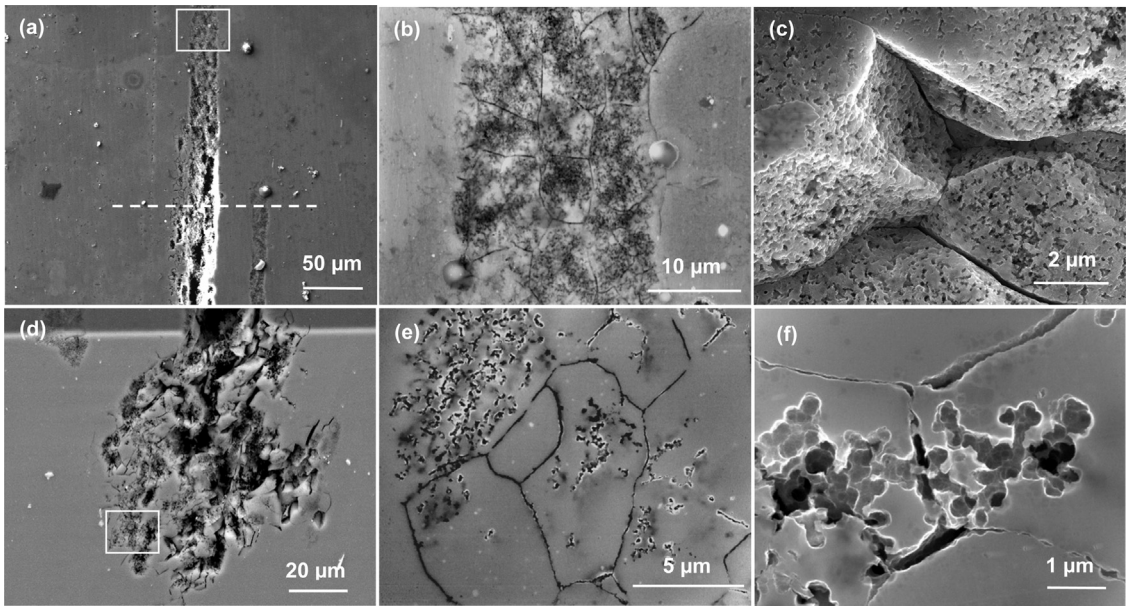

Fig. 1. Secondary electron micrographs of a typical localised corrosion site in AA 2099-T83 alloy after immersion in 3.5% NaCl solution for 5 h: (a) general view of the localised corrosion site; (b) the framed region in (a) at increased magnificaiton; (c) cross-sectional view of the attacked grains in (b); (d) ultramicrotomed cross section from the dashed line in (a); and (e, f) detailed morphology in the framed region in (d).

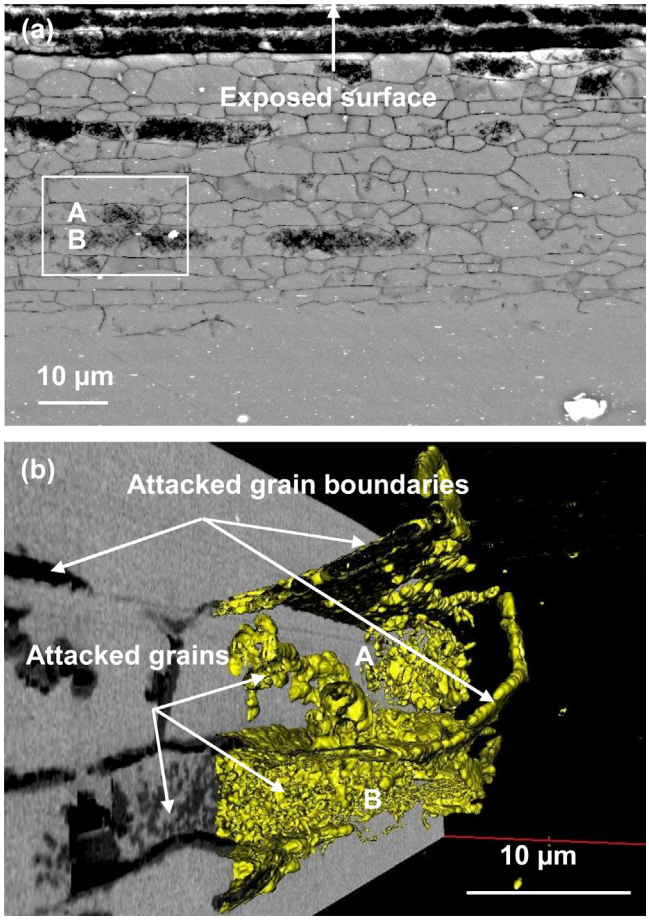

Fig. 2. (a) A backscattered electron micrograph of the cross section of AA 2099-T83 alloy after polarization from −0.767 to 0.824 V(SCE) in 3.5% NaCl solution; and (b) 3D volumetric reconstruction of the framed region in (a), with selective transparency applied to the aluminium matrix and yellow colour applied to corrosion product. The observed section corresponds to the long transverse section of the extrusion. (For interpretation of the references to colour in this figure legend, the reader is referred to the web version of this article).

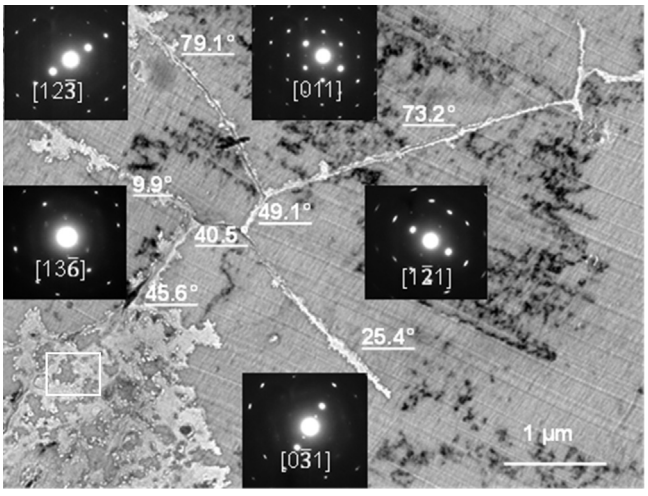

Fig. 3. Transmission electron micrograph of an ultramicrotomed alloy section after immersion in deionized water for 10 min, revealing preferentially attacked grain boundaries and grain interiors during the period of immersion. Inserts are diffraction patterns obtained from each grain, giving the orientation of the grains. The observed alloy section corresponds to the short transverse section of the extrusion.

et al. [6] on AA 2050-T83 alloy indicated preferential corrosion of grains oriented with (1 1 1) planes exposed to the electrolyte. The authors related the corrosion susceptibility to more negative corrosion potential of these grains than grains oriented with other planes exposed to the electrolyte. However, it seems difficult to explain the selective corrosion of grains beneath the alloy surface and the network or parallel-line corrosion paths within corroded grains in AA 2099-T83 alloy [11–13].

Therefore, in this paper, the origin of the second type localised corrosion in AA 2099-T83 alloy is investigated. In order to accelerate the corrosion process, simulated sea water (3.5% NaCl solution) is selected as the corrosion media. It is found that the localised corrosion tends to occur in the grain with relatively large Schmid factor (relative to the direction of extruding/stretching) and is related to selective dissolution T_1 phase that preferentially precipitates at grain/subgrain boundaries and dislocations within grain

interiors. Based on the findings and the thermomechanical history of the alloy, the mechanism for the localised corrosion in AA 2099-T83 alloy during exposure to 3.5% NaCl solution is discussed.

2. Experimental procedure

Specimens, of $30 \times 20 \times 5\ mm^3$, were prepared from the middle of an extruded T-shaped beam of AA 2099-T83 aluminium alloy (1.62 wt.% Li; 2.83 wt.% Cu; 0.72 wt.% Zn; 0.30 wt.% Mg; 0.29 wt.% Mn; 0.04 wt.% Fe; 0.06 wt.% K; 985 ppm Zr; 180 ppm Si; 1.5 ppm Ag; remainder, Al). The specimens were successively ground with 800, 1200 and 4000 grit silicon carbide papers and polished sequentially using 6, 3 and 1 μm diamond pastes with Mecaprex polishing liquid as lubricant. Following mechanical polishing, the specimens were degreased in acetone, rinsed in deionised water and dried in a cold air stream. The specimens were then ready for corrosion testing. The tested surfaces correspond to the longitudinal plane of the extrusion except stated elsewhere.

Three types of corrosion testing were performed. Conventional immersion testing was carried out in a 250 mL glass beaker containing 150 mL 3.5 wt.% NaCl solution at ambient temperature (15 ~ 20 °C) for 5 h. Under such condition, typical localised corrosion was observed. Another polished specimen was polarized from −0.767 to 0.824 V(SCE) at a scanning rate of 0.5 mV/s using a Solartron 1287 potentiostat. The cell geometry is the same as that used for immersion testing. Under such condition, localised corrosion beneath the exposed surface was observed. Observing corrosion attack beneath the exposed surface is important because the influence of sample surface condition can be reduced. In addition, alloy slices of 15 nm nominal thickness were generated from the polished specimen using ultramicrotomy and left in water bath behind the diamond knife (filled with deionised water) for 10 min. Under such condition, localised corrosion in its early stage was observed. Such specimens also facilitate examining corrosion morphology and crystallographic structures of related regions by transmission electron microscopy (TEM).

Surfaces and cross-sections of the tested specimens were examined in Phillips XL 30 and Zeiss Ultra 55 field emission gun scanning electron microscopes (FEG-SEMs), fitted with energy dispersive X-ray (EDX) and electron backscattered diffraction (EBSD) facilities. In order to acquire EBSD data from the corroded area, the corroded specimens were further etched in 20 wt.% NaOH solution at room temperature for 60 s, and then desmutted in 30 vol.% HNO_3 solution for 30 s, rinsed in deionised water and dried in a cold air stream. VMAP software developed in-house at Manchester and HKL Channel 5 (Oxford instrument) were used to process EBSD data acquired by the Zeiss Ultra 55 FEG-SEM. Particularly, grain orientations, grain/subgrain boundaries and Schmid factors of grains were calculated. Schmid factor is expressed as $m = \cos\lambda \cos\varphi$, where λ is the angle between the direction of the applied force and the slip direction; φ is the angle between the direction of the external force and the normal direction of the slip plane. Given the direction of the external force, the Schmid factor is solely determined by the grain orientation. The value of the Schmid factor is between 0 and 0.5.

For characterisation of the alloy microstructure, electron transparent foils were prepared by twin-jet electropolishing in a Tenupol-3 instrument at 20 V in a mixed solution of 30 vol.% nitric acid and 70 vol.% methanol at about −30 °C. Bright field TEM images were taken on a Joel 2000 FXII transmission electron microscope, operated at an accelerating voltage of 120 kV; high resolution lattice images and high angle annular dark field (HAADF) images (Z-contrast) were taken on a FEI Tecnai G^2 F30 instrument, operated at an accelerating voltage of 300 kV.

3. Results

A typical localised corrosion site, of ~1 mm length and tens of micrometres width, is observed on the specimen after immersion in 3.5% NaCl solution for 5 h, as shown in Fig. 1(a). Focusing on the framed region in Fig. 1(a), Fig. 1 (b) shows selective attack of grain boundaries and grain interiors in an elongated region. The cross sectional view of the attacked grains shows corrosion paths within the grains (Fig. 1(c)). An ultramicrotomed cross section of the localised corrosion site along the dashed line indicated in Fig. 1(a) is displayed in Fig. 1(d). It is evident that the localised corrosion propagates from the alloy surface deep into the alloy via particular paths. Examination of corrosion fronts at increased magnification (Fig. 1(e) and (f)) indicates that the severity of corrosion varies from grain to grain and preferential corrosion paths are present within attacked grains.

Extensive corrosion occurs on the specimen subjected to potentiodynamic polarization from −0.767 to 0.824 V(SCE). Selective attack of grain boundaries and grain interiors is observed on the cross section of the specimen tens of micrometres beneath the exposed surface (Fig. 2(a)). SEM-based tomography [18,19] is conducted on the framed region in Fig. 2(a), with selective transparency applied to the aluminium matrix and yellow colour applied to corrosion product. Fig. 2(b) shows the 3-dimensitonal reconstruction of the corroded grain boundaries and grain interiors, revealing the different extent of grain interior attack with the two most severely attacked grains being labelled with A and B. Since almost all grain boundaries in the imaged region in Fig. 2(a) are corroded, all the grains between the corroded grain boundaries are exposed to similar corrosion conditions. Therefore, it is suggested that the selectively corroded grains are intrinsically different from other grains.

Fig. 3 shows a bright field TEM image taken from an ultramicrotomed section after immersion in deionized water for 10 min, again revealing preferentially attacked grain boundaries and grain interiors. The grain orientations and the misorientations between grains, as labelled, are determined by electron diffraction. Most of the attacked grain boundaries are determined to be high angle grain boundaries (HAGBs) ($\theta > 15°$), with only one low angle grain boundaries (LAGBs) ($<15°$) being found in the examined area. Additionally, some grains (e.g. $[0\bar{3}1]$ grain) are more susceptible to corrosion than other grains. Detailed microstructure of the corroded area in $[0\bar{3}1]$ grain is shown in Fig. 4. Bright fringes are revealed at the interface between the attacked regions and the intact alloy matrix (Fig. 4(a)), corresponding to enrichment of copper which is frequently observed during anodizing, electropolishing or chemical etching of copper-containing alloys [20–26]. Further, bright nanoparticles of ~5 nm in diameter are detected in the corrosion product (Fig. 4(b)). The copper-rich nanoparticles are either pure copper (cubic, a = 0.361 nm) or θ″ (Al_2Cu) phase (tetragonal, a = b = 0.404 nm, c = 0.768 nm), as suggested by the lattice images (Fig. 4(c) and (d)). Previous work [27–29] indicates that copper-rich nanoparticles formed in the copper-enriched layer during anodizing of copper-containing aluminium alloys are θ' (Al_2Cu) phase. Therefore, it is suggested that the θ″ (Al_2Cu) phase particle found in the corrosion product is from the copper-enriched layer developed during corrosion of the alloy matrix. The copper nanoparticles, however, should be generated in a different way, e.g. dealloying of T_1 phase. The dealloying process of T_1 phase has not been systematically investigated so far. However, it is reported that copper remnant can be formed as a consequence of dealloying of S (Al_2CuMg) phase [30].

In order to obtain more microstructural information from the region where localised corrosion occurred, EBSD analysis is performed on a typical localised corrosion site (Fig. 5(a)). Different grains are displayed in different colours, with subgrain boundaries

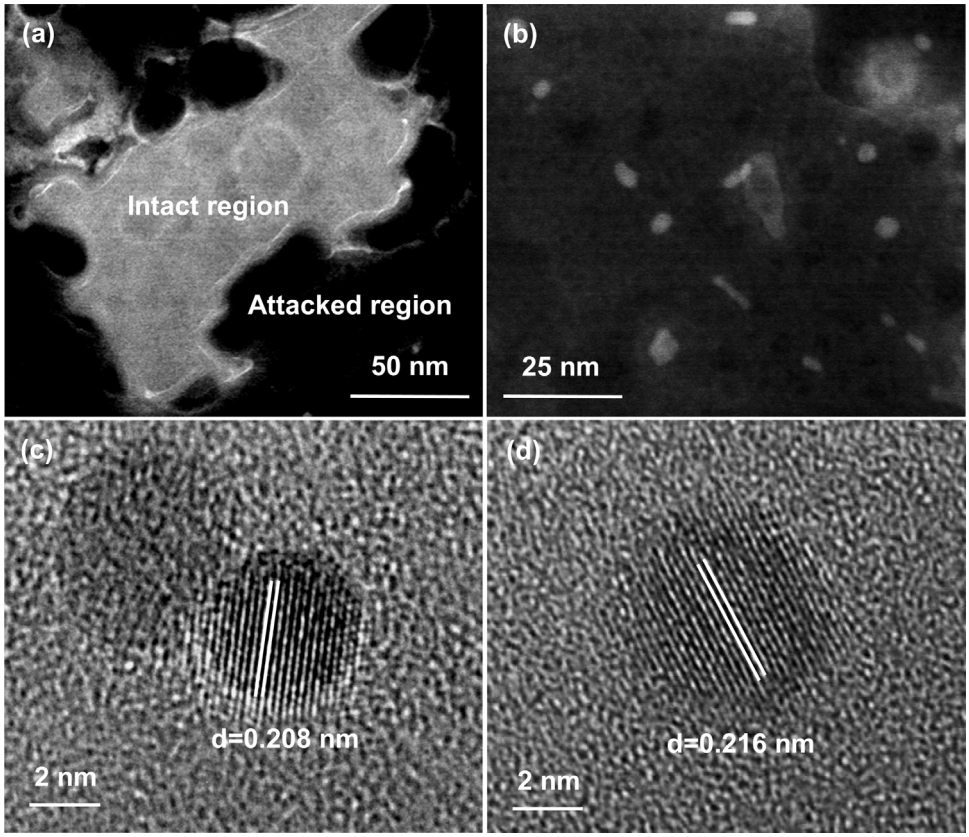

Fig. 4. HAADF images (Z-contrast) taken from the framed region in Fig. 3, showing (a) copper-enriched layer at the interface between the intact and the attacked regions and (b) copper-rich nanoparticles in corrosion product; and lattice images of copper-rich nanoparticles in (b), showing (c) (111) planes of Cu and (d) (013) planes of θ″ (Al_2Cu) phase.

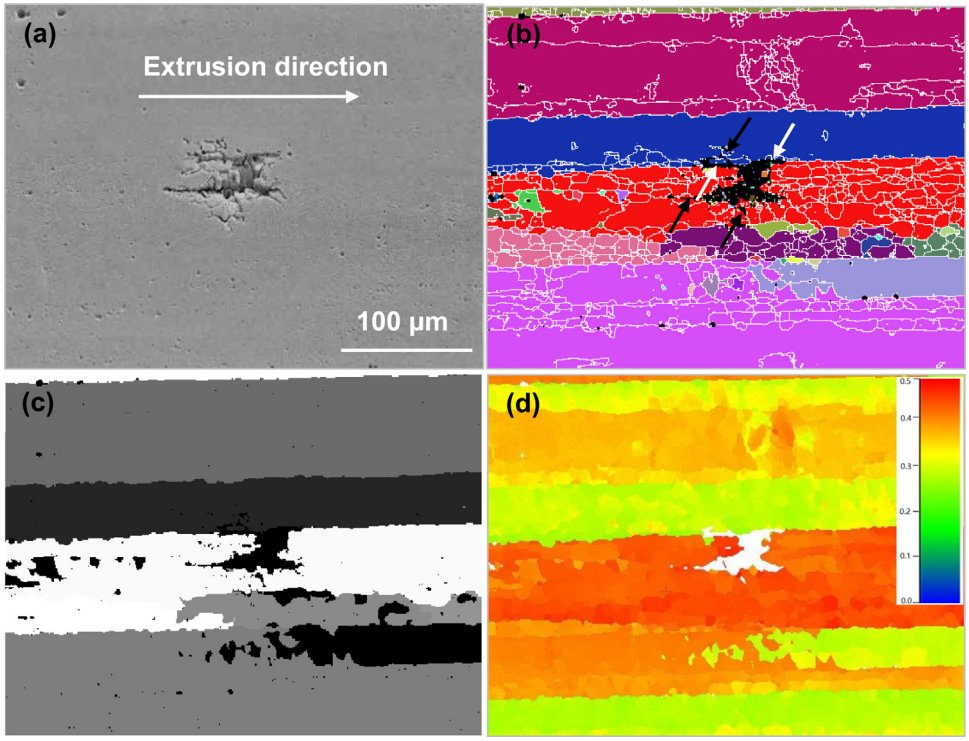

Fig. 5. EBSD analysis of the region containing a typical localised corrosion site: (a) secondary electron micrograph; (b) distribution of grains and subgrains; (c) stored energy of grains; and (d) Schmid factors of grains.

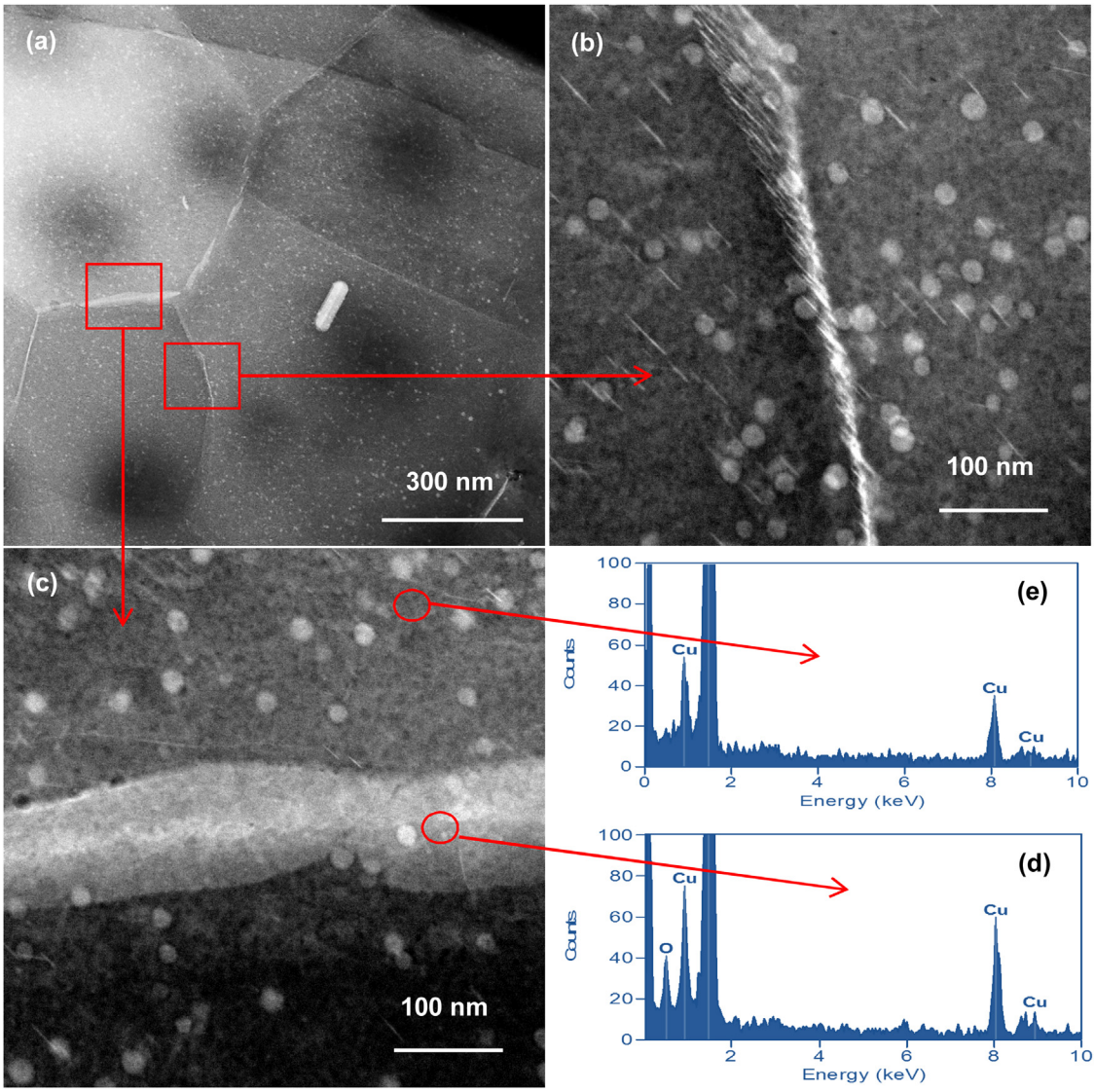

Fig. 6. (a–c) HAADF images (Z-contrast) of the twin-jet electropolished AA 2099-T83 alloy showing grain boundary precipitates; and (d, e) EDX spectra obtained from the coarse precipitate and alloy matrix.

being superimposed on the same image as white lines (Fig. 5(b)). It is found that the major proportion of the localised corrosion site is confined in the red grain. Propagation of corrosion along grain boundaries (indicated by the white arrows) and subgrain boundaries (indicated by the black arrows) is evident. The distribution of grain stored energy [12] is shown in Fig. 5(c), where grains with relatively high stored energy are displayed in relatively light colours. Coincidently, the grain containing the localised corrosion site shows the highest stored energy. Further, Schmid factors of grains (relative to the direction of extruding/stretching) are calculated and mapped (Fig. 5(d)). The Schmid factor of the grain containing the localised corrosion site is between 0.4 and 0.5, much larger than those of other grains. Note that Schmid factors of subgrains also slightly vary. As discussed later, these findings together with subsequent microstructure characterization of the alloy in next section provide solid evidence showing the origin of localised corrosion developed in AA 2099-T83 alloy after immersion in 3.5% NaCl solution.

The distribution of grain boundary precipitates in the alloy is revealed in the HADDF image (Fig. 6(a)). Most of the grain boundary precipitates are T_1 phase (Fig. 6(b)) [1,9,10]. In addition, coarse precipitates are also observed at grain boundaries (Fig. 6(c)). EDX spectrum obtained from the coarse precipitate (Fig. 6(d)) shows increased level of copper and oxygen compared with the alloy matrix (Fig. 6(e)), suggesting that the coarse precipitate is rich in copper and highly reactive to the environment. Probably such coarse grain boundary precipitate is coarsened T_1 phase; or it is T_2 (Al_6CuLi_3) phase that is found at grain boundaries in AA 8090 and AA 2090 [1]. The white, spherical particles are Al_3Zr dispersoid [17]. The high population density of Li-containing precipitates at grain boundaries explains the high susceptibility of the alloy to intergranular corrosion.

Fig. 7(a) is a dark field TEM micrograph imaged by using the $(10\bar{1}0)$ diffraction spot of T_1 phase, revealing distribution of T_1 phase at subgrain boundaries (the misorientation angle $\theta < 1$) and dislocations. The population density of T_1 phase at subgrain boundaries and dislocations is much higher than that in bulk alloy matrix (Fig. 7(b)). Such preferential precipitation of T_1 phase at crystallographic defects explains preferential corrosion in grain interiors.

4. Discussion

The results suggest that selective corrosion of grain/subgrain boundaries and grain interiors at localised corrosion site is related

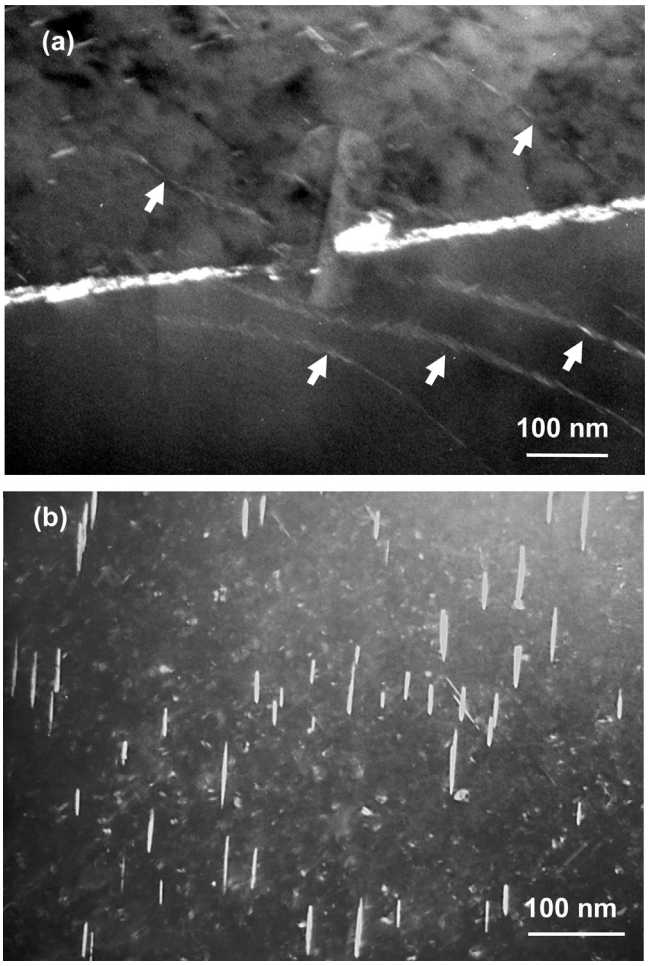

Fig. 7. Dark field transmission electron micrographs of the twin-jet electropolished AA 2099-T83 alloy: (a) heterogeneous distribution of T_1 phase at low angle grain boundaries and dislocation lines; and (b) homogeneous distribution of T_1 phase within the alloy matrix.

to preferential precipitation of T_1 phase at grain/subgrain boundaries and dislocations. For the present study corrosion likely starts by dealloying of T_1 phase, leading to the formation of copper-rich remnants. Allowing these remnants to act as cathodes, the dealloyed T_1 phase drives anodic dissolution of the surrounding alloy matrix. Meanwhile the copper-enriched layer and copper-rich nanoparticles arising from corroded alloy matrix provide additional cathodic sites.

The reason why localised corrosion prefers particular grains in AA 2099-T83 alloy deserves further discussion by considering the thermomechanical history of the alloy and the EBSD results. The alloy is artificially aged to obtain designed mechanical properties. Before artificial ageing, the extruded profile is firstly solution treated to obtain a super-saturated solution, which is necessary for artificial ageing. Additionally, in order to restrict excessive precipitation of T_1 phase at grain boundaries, the solution treated alloy is further cold stretched along the extrusion direction (at 3% elongation) to increase dislocations within grain interiors and, therefore, to promote the precipitation of T_1 phase within grain interiors during ageing [31,32]. It is known that the capability of plastic deformation of each grain in polycrystalline materials, governed by the Schmid factor of each grain, is different. At low or medium strain, it is impossible for all grains to experience similar degrees of plastic deformation and the grains with large Schmid factors must experience more plastic deformation than other grains [33–36]. Consequently, dislocation density in these grains must be higher than other grains. Increased dislocation density means increased population density or volume fraction of T_1 phase after artificial ageing. The corrosion potential of T_1 phase in 3.5 wt.% NaCl solution is −1096 mV(SCE) [31], which is 346 mV more negative than that of aluminium matrix (−750 mV(SCE) [37]). Due to the high electrochemical activity of T_1 phase, the grains containing higher population density or volume fraction of T_1 phase become more susceptible to corrosion than other grains.

Fig. 8 schematically illustrates how localised corrosion develops in such a grain. Give three neighbouring grains A, B and C, where Grain B has much larger Schmid factor than Grains A and C (Fig. 8(a)). When cold stretching the alloy along the extrusion

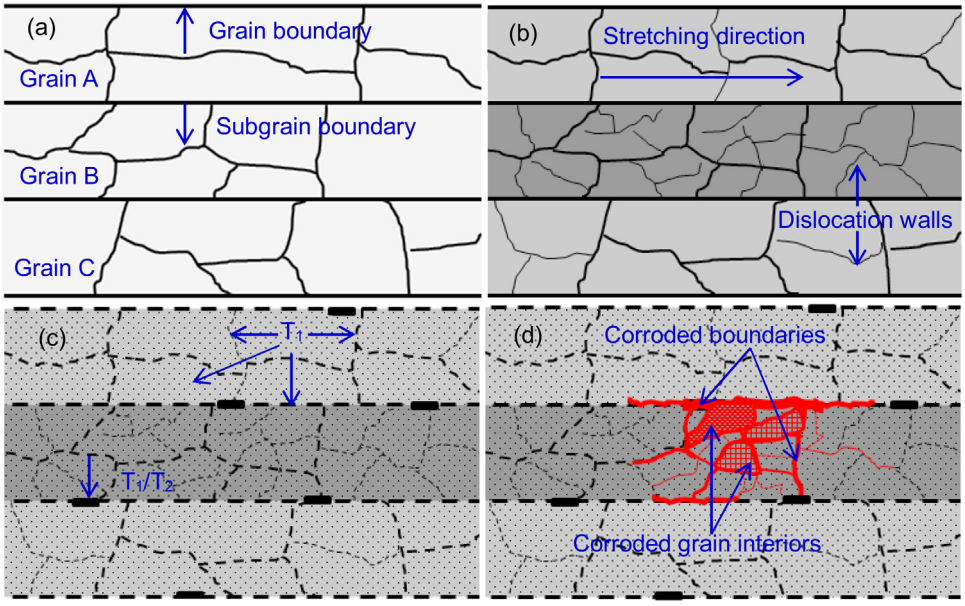

Fig. 8. Schematic diagrams showing the correlation between thermomechanical history of AA 2099-T83 alloy and typical localised corrosion developed in the alloy: (a) typical microstructure after extrusion and solution treatment; (b) typical microstructure after cold stretching (the grey scale indicates dislocation density within the alloy matrix); (c) typical microstructure after artificial ageing (the grey scale indicates not only dislocation density but also the density or volume fraction of T_1 phase within the alloy matrix); and (d) development of the localised corrosion.

direction, all the three grains are plastically deformed, with Grain B experiencing much more plastic deformation than the other two grains. Consequently, dislocations increase in the grains and more subgrain boundaries/dislocation walls are formed (Fig. 8(b)). The dislocation density in each grain is indicated by the grey scale, with the darker grain (Grain B) containing more dislocations. During artificial ageing, T_1 phase nucleates and grows at both grain/subgrain boundaries and dislocations within grain interiors, with the kinetics of nucleation and growth being influenced by the energy of crystallographic defects. This results in heterogeneous distribution of T_1 phase (Fig. 8(c)). Note that the grey scale in Fig. 8(c) reflects not only dislocation density but also the density or volume fraction of T_1 phase. When the surfaces of the three grains are exposed to corrosive environment, localised corrosion is preferentially developed in Grain B. Once localised corrosion initiates in Grain B, the galvanic coupling effect between Grain B and Grains A and C renders the corrosion process proceeding mainly in Grain B. Thereafter, localised corrosion propagates in Grain B along preferred paths such as grain/subgrain boundaries and dislocation walls (Fig. 8(d)). When the corrosion event propagates beneath the alloy surface, the narrow, network corrosion paths can restrict access of bulk solution to corrosion fronts, leading to building up of Cl^- and H^+ at corrosion fronts. The acidic, chloride-rich environment at corrosion fronts prevents the corroding alloy from repassivating, leading to continuous propagation of the corrosion event.

5. Conclusions

1) The localised corrosion in AA 2099-T83 alloy, typified by selective attack of grain/subgrain boundaries and individual grain interiors, is related to selective dissolution of T_1 phase preferentially precipitates at the grain/subgrain boundaries and dislocations within the grain interiors.
2) Schmid factor can directly indicate corrosion susceptibility of the grain/subgrain in AA 2099-T83 alloy, with localised corrosion preferentially occurring in the grain with large Schmid factor.
3) The grain with relatively large Schmid factor will experience more plastic deformation than other grains when subjected to cold stretching prior to artificial ageing. High dislocation density (or stored energy) in the grain with large Schmid factor will lead to increased density or volume fraction of T_1 phase after artificial ageing. High electrochemical activity of T_1 phase results in development of localised corrosion in the grain with large Schmid factor in corrosive environment.

Acknowledgements

The authors wish to gratefully acknowledge the National Natural Science Foundation of China (Grant Nos. 51301214, 51541102, 51275037), Fundamental and Cutting-edge Research Plan of Chongqing (Grant No. cstc2013jcyjA50017) and EPSRC LATEST2 Program Grant.

References

[1] N.E. Prasad, A.A. Gokhale, R.J.H. Wanhill, Aluminum-Lithium Alloys, first ed., Elsevier, Amsterdam, 2014.
[2] C. Kumai, J. Kusinski, G. Thomas, T.M. Devine, Influence of aging at 200 °C on the corrosion of Al-Li and Al-Li-Cu alloys, Corrosion 45 (1989) 294–302.
[3] R.G. Buchheit, J.P. Moran, G.E. Stoner, Localised corrosion behavior of alloy 2090-the role of microstructural heterogeneity, Corrosion 46 (1990) 610–617.
[4] R.G. Buchheit, J.P. Moran, G.E. Stoner, Electrochemical behavior of the T1(Al2CuLi) intermetallic compound and its role in localised corrosion of Al-2%Li-3% Cu Alloys, Corrosion 50 (1994) 120–130.
[5] J.F. Li, Z.Q. Zheng, S.C. Li, W.J. Chen, W.D. Ren, X.S. Zhao, Simulation study on function mechanism of some precipitates in localised corrosion of Al alloys, Corros. Sci. 49 (2007) 2436–2449.
[6] M. Guérin, J. Alexis, E. Andrieu, L. Laffont, W. Lefebvre, G. Odemer, C. Blanc, Identification of the metallurgical parameters explaining the corrosion susceptibility in a 2050 aluminium alloy, Corros. Sci. 102 (2016) 291–300.
[7] V. Proton, J. Alexis, E. Andrieu, J. Delfosse, A. Deschamps, F. De Geuser, M.C. Lafont, C. Blanc, The influence of artificial ageing on the corrosion behaviour of a 2050 aluminium-copper-lithium alloy, Corros. Sci. 80 (2014) 494–502.
[8] V. Proton, J. Alexis, E. Andrieu, J. Delfosse, M.C. Lafont, C. Blanc, Characterisation and understanding of the corrosion behavior of the nugget in a 2050 aluminium alloy friction stir welding joint, Corros. Sci. 73 (2013) 130–142.
[9] R.G. Buchheit, D. Mathur, P.I. Gouma, Corrosion and Corrosion Prevention of Low Density Metals and Alloys, in: B.A. Shaw, R.G. Buchheit, J.P. Moran (Eds.), The Electrochemical Society, Pennington, New Jersey, 2001, pp. 444–452.
[10] J.E. Kertz, P.I. Gouma, R.G. Buchheit, Localised corrosion susceptibility of Al-Li-Cu-Mg-Zn alloy AF/C458 due to interrupted quenching from solutionizing, Metall. Mater. Trans. A 32 (2001) 2561–2573.
[11] W. Huang, Y. Ma, X. Zhou, X. Meng, Y. Liao, L. Chai, Y. Yi, X. Zhang, Correlation between localised plastic deformation and localised corrosion in AA2099 aluminum-lithium alloy, Surf. Interface Anal. (2016), http://dx.doi.org/10.1002/sia.5817,2015.
[12] Y. Ma, X. Zhou, W. Huang, Y. Liao, X. Chen, X. Zhang, Crystallographic defects induced localised corrosion in AA2099-T8 aluminium alloy, Corros. Eng. Sci. Technol. 50 (2015) 420–424.
[13] Y. Ma, X. Zhou, W. Huang, G.E. Thompson, X. Zhang, C. Luo, Z. Sun, Localised corrosion in AA2099-T8 aluminum-lithium alloy: the role of intermetallic particles, Mater. Chem. Phys. 161 (2015) 201–210.
[14] A. Hughes, T.H. Muster, A. Boag, A.M. Glenn, C. Luo, X. Zhou, G.E. Thompson, D. McCulloch, Co-operative corrosion phenomena, Corros. Sci. 52 (2010) 665–668.
[15] A. Boag, R.J. Taylor, T.H. Muster, N. Goodman, D. McCulloch, C. Ryan, B. Rout, D. Jamieson, A.E. Hughes, Stable pit formation on AA2024-T3 in a NaCl environment, Corros. Sci. 52 (2010) 90–103.
[16] A. Boag, A.E. Hughes, A.M. Glenn, T.H. Muster, D. McCulloch, Corrosion of AA2024-T3 part I: localised corrosion of isolated IM particles, Corros. Sci. 53 (2011) 17–26.
[17] Y. Ma, X. Zhou, G.E. Thompson, T. Hashimoto, P. Thomson, M. Fowles, Distribution of intermetallics in an AA2099-T8 aluminium alloy extrusion, Mater. Chem. Phys. 126 (2011) 46–53.
[18] T. Hashimoto, X. Zhou, C. Luo, K. Kawano, G.E. Thompson, A.E. Hughes, P. Skeldon, P.J. Withers, T.J. Marrow, A.H. Sherry, Nantomography for understanding materials degradation, Scr. Mater. 63 (2010) 835–838.
[19] X. Zhou, C. Luo, T. Hashimoto, A. Hughes, G.E. Thompson, Study of localised corrosion in AA2024 aluminium alloy using electron tomography, Corros. Sci. 58 (2012) 299–306.
[20] X. Zhou, G.E. Thompson, H. Habazaki, K. Shimizu, P. Skeldon, G.C. Wood, Copper enrichment in Al-Cu alloys due to electropolishing and anodic oxidation, Thin Solid Films 293 (1997) 327–332.
[21] Y. Liu, E.A. Sultan, E.V. Koroleva, P. Skeldon, G.E. Thompson, X. Zhou, K. Shimizu, H. Habazaki, Grain orientation effects on copper enrichment and oxygen generation during anodizing of an Al-1at.%Cu alloy, Corros. Sci. 45 (2003) 789–797.
[22] Y. Liu, F. Colin, P. Skeldon, G.E. Thompson, X. Zhou, H. Habazaki, K. Shimizu, Enrichment factors for copper in aluminium alloys following chemical and electrochemical surface treatments, Corros. Sci. 45 (2003) 1539–1544.
[23] Y. Liu, M.A. Arenas, P. Skeldon, G.E. Thompson, H. Habazaki, K. Shimizu, P. Bailey, T.C.Q. Noakes, Generation of copper nanoparticles during alkaline etching of an Al-30at.%Cu alloy, Corros. Sci. 48 (2006) 1874–1884.
[24] Y. Liu, M.A. Arenas, S.J. Garcia-Vergara, T. Hashimoto, P. Skeldon, G.E. Thompson, H. Habazaki, P. Bailey, T.C.Q. Noakes, Behaviour of copper during alkaline corrosion of Al-Cu alloys, Corros. Sci. 50 (2008) 1475–1480.
[25] Y. Ma, X. Zhou, G.E. Thompson, P. Skeldon, Surface texture formed on AA2099 Al–Li–Cu alloy during alkaline etching, Corros. Sci. 66 (2013) 292–299.
[26] Y. Ma, X. Zhou, G.E. Thompson, X. Zhang, C. Luo, M. Curioni, H. Liu, Microstructural modification arising from alkaline etching and its effect on anodizing behavior of Al-Li-Cu alloy, J. Electrochem. Soc. 160 (2013) C111–C118.
[27] Y. Ma, X. Zhou, G.E. Thompson, M. Curioni, T. Hashimoto, P. Skeldon, P. Thomson, M. Fowles, Anodic Film formation on AA2099-T8 aluminium alloy in tartaric-sulphuric acid, J. Electrochem. Soc. 158 (2011) C17–C22.
[28] Y. Ma, X. Zhou, G.E. Thompson, M. Curioni, T. Hashimoto, P. Skeldon, E. Koroleva, Single-step fabrication of metal nanoparticle loaded mesoporous alumina through anodizing of a commercial aluminum alloy, Electrochem. Solid-State Lett. 15 (2012) E4–E6.
[29] T. Hashimoto, X. Zhou, P. Skeldon, G.E. Thompson, Structure of the Copper–Enriched layer introduced by anodic oxidation of copper-Containing aluminium alloy, Electrochim. Acta 179 (2015) 394–401.
[30] T. Hashimoto, X. Zhang, X. Zhou, P. Skeldon, S.J. Haigh, G.E. Thompson, Investigation of dealloying of S phase (Al2CuMg) in AA 2024-T3 aluminium alloy using high resolution 2D and 3D electron imaging, Corros. Sci. (2016), http://dx.doi.org/10.1016/j.corsci.2015.11.013.
[31] R.G. Buchheit, A compilation of corrosion potentials reported for intermetallic phases in aluminum alloys, J. Electrochem. Soc. 142 (1995) 3994–3996.
[32] R. Yoshimura, T.J. Konno, E. Abe, K. Hiraga, Transmission electron microscopy study of the evolutin of precipitates in aged Al-Li-Cu alloy: the θ' and T1 phases, Acta Mater. 51 (2003) 4251–4266.

[33] Q. Liu, D.J. Jensen, N. Hansen, Effect of grain orientation on deformation structure in cold-rolled polycrystalline aluminum, Acta Mater. 46 (1998) 5819–5838.
[34] N. Hansen, D.J. Jensen, Development of microstructure in FCC metals during cold work, Philos. Trans. R. Soc. A 357 (1999) 1447–1469.
[35] A. Godfrey, N. Hansen, D.J. Jensen, Microstructure-based measurement of local stored energy variation in deformation metals, Metall. Mater. Trans. A 38 (2007) 2329–2339.
[36] Q. Liu, Z.Y. Yao, A. Godfrey, W. Liu, Effect of particles on microstructural evolution during cold rolling of the aluminum alloy AA3104, J. Alloys Compd. 482 (2009) 264–271.
[37] C. Vargel, translated by M. P. Schmidt, Corrosion of Aluminum, first ed., Elsevier Amsterdam, 2004.